Multi-strange baryon spectroscopy at the LHCb experiment in $\Omega_c^0 \to \Xi^- K^- \pi^+ \pi^+$ decays

Author: Carla Garcia Gazulla
Facultat de Física, Universitat de Barcelona, Diagonal 645, 08028 Barcelona, Spain.

Advisor: Carla Marín Benito and Lukas Calefice

Abstract: In this study, the decay $\Omega_c^0 \to \Xi^- K^- \pi^+ \pi^+$ is analysed to search for the presence of excited Ω^- baryon states. Using data from the LHCb experiment, a Boosted Decision Tree (BDT) classifier is developed, enhancing the signal-to-background ratio by a factor 2 compared to standard selection criteria. This approach resulted in a clean Ω_c^0 mass peak, enabling the exploration of excited states. The invariant mass spectra reveal hints of a potential resonance.
Keywords: High energy physics, Data Analysis, machine learning, strange particles, spectroscopy
SDGs: Industry, innovation and infrastructure

I. INTRODUCTION

Spectroscopy of baryons in the strange sector hold valuable clues for advancing our understanding of hadronic physics. Despite significant progress in the heavy-flavour sector [1][2], theoretical predictions and experimental studies in the low-mass flavour sector remain limited, with little advancement since the 1980s. This gap highlights the need for focused exploration to uncover the properties of these particles and their excited states.

Using data from the LHCb experiment, this project seeks to enhance the signal-to-background ratio to identify the excited states of the Ω^- baryon more effectively, by studying its resonance spectrum through the decay $\Omega_c^0 \to \Xi^- K^- \pi^+ \pi^+$.

Four excited Ω^- states have been observed so far: $\Omega^-(2250)$ [3][4], $\Omega^-(2380)$ [3], and $\Omega^-(2470)$ [5] in fixed-target experiments in the 1980s, and more recently, $\Omega^-(2012)$ [6], by the BELLE collaboration, which is not expected to be accessible with our decay mode. However, most of them were observed with low statistics and have not been experimentally confirmed. Experiments such as GlueX, J-PARC, and PANDA are aiming to explore strange baryon spectroscopy in the future.

Beyond its immediate scope, this work could support future studies, such as reducing systematic uncertainties in pentaquark searches or investigating potential contributions of New Physics (NP) in the strange decays of Ω_b and Ξ_b.

II. LHCB

LHCb is one of the four experiments based at the CERN's Large Hadron Collider (LHC) [8]. Within its detector, two beams of protons travelling in opposite directions are collided, producing a wide variety of particles. LHCb specializes in studying the decays of hadrons containing b or c quarks.

The LHCb experiment has several sub-detectors, each optimized to measure specific characteristics of the particles produced. These detectors are categorized into two main groups: tracking detectors (VELO, TT, and tracking stations) and Particle Identification (PID) detectors.

When a charged particle is produced, it interacts with the various layers of the tracking system, leaving signals that can be used to reconstruct its trajectory. The curvature of the trajectory, caused by the magnetic field of a dipole magnet, allows for a measurement of the particle's momentum. Additionally, the VELO is designed to precisely measure the positions of primary and secondary vertices (PV, SV). If the particle interacts with the VELO, its trajectory is classified as a "long track" (L); otherwise, it is classified as a "downstream track" (D).

Finally, to distinguish between charged hadrons, Ring Imaging Cherenkov (RICH) detectors use the Cherenkov effect to measure particle's velocity. By combining velocity and momentum, particles can be identified based on their mass.

A. Decay of interest

In the decay process being studied, a heavy-flavour Ω_c^0 baryon decays into lighter hadrons via weak interactions. The decay chain is:

$$\Omega_c^0 \to \Xi^-(\to \Lambda^0(\to p\pi^-)\pi^-)K^-\pi^+\pi^+$$

The excited states of Ω^- are expected to decay into Ξ^-, π^+, and K^- particles. If such a state exists, it would be short-lived and appear as a peak in the invariant mass projection of its decay products.

The decay chain involves three vertices. While the Ω_c^0 baryon is relatively stable, it mainly decays inside the VELO, so the two π^+ and the K^- from the Ω_c^0 decay are always L tracks. On the other hand, Ξ^- and Λ^0 particles have large lifetimes, and therefore, a probability of decaying either inside or outside the VELO. Based on the tracks of the two π^- and the proton from the Ξ^- decay, events are classified into three types: DDD, DDL, and LLL. The diagram of the DDL topology is shown in Fig. 1.

Each track type has its strengths and weaknesses. LLL category has much better track reconstruction, as the VELO captures detailed information of all the vertices.

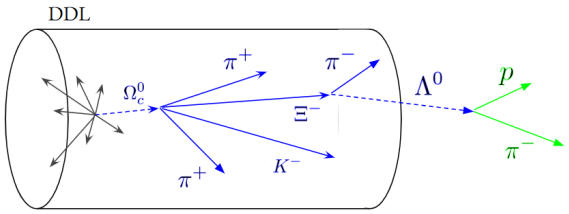

FIG. 1: DDL decay distribution in the VELO. Blue lines represent L tracks and green ones, D tracks. Dashed lines represent neutral particles, which do not leave signal in the detector.

Additionally, it provides higher resolution momentum measurements. However, it has fewer events compared to the other track types due to the large lifetimes of Ξ^- and Λ^0. Moreover, it tends to have a higher level of combinatorial background, as a large portion of particles produced in the *pp* collision are L track pions.
Conversely, in the DDD category, the combinatorial background is significantly reduced. However, despite having more signal events initially, a substantial portion is lost during the track combination process.
The DDL category provides a balance between these extremes. Although there is still a significant amount of background, a higher number of signal events is retained compared to DDD. For the remainder of this project, the analysis is focused on the DDL track data, as it appears to be the most promising for achieving results.
Momentum resolution behaviour is illustrated in App.A. Figures 9 and 10, which show the simulated signal distribution for each track type for the variables Ξ^- and Ω_c^0 mass.

B. Data selection

This analysis is performed using data from the full LHCb Run 2, corresponding to an integrated luminosity of approximately 5.6 fb^{-1}. Data from the antiparticle decay is also included, as it is expected to exhibit similar behavior.

The initial dataset is filtered by a trigger system designed to identify Ξ^- particles. Offline processing combines this data with random pions and kaons from the same *pp* collision event, trying to connect the tracks and form vertices. However, since many pions are directly produced at the Primary Vertex, there is a considerable probability of misattributing a pion, leading to a lot of combinatorial background.

Studying this specific decay presents additional challenges. First, Ω_c^0 cross-section is much lower compared to lighter charm hadrons. Moreover, Ω_c^0 usually decay into two particles, not four, so our decay is quite rare. These factors, combined with the difficulty of reconstructing six final tracks properly, result in a lower yield of signal events.

Simulations are used to study the physical behavior of the signal. However, the available simulation was originally generated for a different purpose, leading to a limited number of events. This scarcity of simulated data introduces statistical limitations into the analysis.

III. FIRST SELECTION

In the initial dataset, there are millions of events, but the background is so large that clearly distinguishing any mass peak is too difficult. To quantify the background, Ω_c^0 mass is used as a reference variable, where signal events exhibit a peak at the measured mass of Ω_c^0, 2695.2 MeV/c^2 [7]. By fitting the histogram of this variable with a Gaussian for the signal and a linear function for the background, their yields can be estimated.

The first approach to reduce the background is to apply selection requirements to the data, taking profit from the variables that most discriminate between signal and background. These cuts are based on physical knowledge of the decay topology and comparing the distributions of variables in the simulation and in a subset of data which only contains background events (outside the Ω_c^0 mass peak). A table with the applied cuts and three plots comparing the signal and background distributions are available in App.B.

One of the key variables is the momentum of the particles. Producing the Ω_c^0 requires a significant amount of energy, so the entire decay have higher energy and momentum than background events, that contain low-energy hadrons emerging from the hadronisation process. Furthermore, the quality of the vertex fit for the SV is expected to be worse for background candidates. This can be observed in variables such as χ^2_{vtx} or χ^2_{IP}, where background events typically show poorer values compared to signal events.

The result of applying these cuts to the data and fitting the signal and background distributions is shown in Fig. 2. The Ω_c^0 peak is pretty clear, and the number of signal candidates is significant enough to continue the analysis, the problem is the high level of background. To further reduce it, the analysis is continued using machine learning.

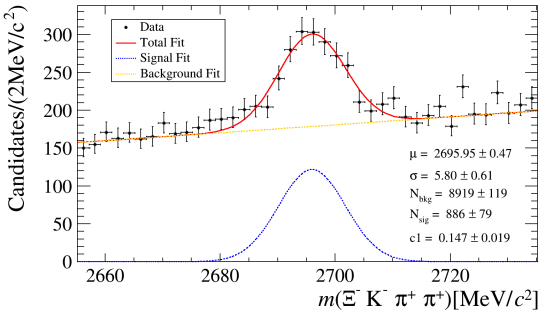

FIG. 2: Fitted Ω_c^0 mass variable with tight cuts applied to the data. Gaussian fit for signal and linear for background.

IV. BDT

Boosted Decision Trees (BDTs) are a type of machine learning algorithm particularly effective for classification and regression tasks. They work by combining the outputs of many weak supervised learners, in this case, decision trees, into a single and accurate predictive model.

In this analysis, we use XGBoost [9], a powerful implementation of gradient-boosted decision trees, designed for supervised learning problems. The training data consists of multiple features used to predict a target variable. In this case, discriminating variables are used to calculate the probability of an event being signal, with values ranging from 0 (100% background) to 1 (100% signal). Based on these probabilities, a selection threshold can be applied to retain events that are more likely to be signal and discard those classified as background.

To train the BDT, labelled data is required: simulated data serves as the signal category, while background is derived from the events outside the Ω_c^0 mass peak. This allows the model to learn patterns that distinguish signal from background effectively.

Due to the limited availability of simulations, the model is trained with 1923 events in each category. App.C, Fig. 15, illustrates the training data.

A. BDT Evaluation

One of the main challenges in using BDTs is to prevent overfitting. With limited training data, it is easy for the BDT to focus excessively on specific features of the training dataset, making it less generalizable to new data.

To assess the BDT's performance and detect overfitting, a portion of the data is reserved as a test set. Performance is evaluated using the probability distribution assigned by the BDT and the Receiver Operating Characteristic (ROC) curve, which plots the True Positive Rate (TPR) against the False Positive Rate (FPR) for different thresholds. The area under the curve (AUC) provides a numerical measure of classification quality, with values closer to 1 indicating better performance.

To optimize the BDT, key internal learning parameters can be adjusted. These include the number of estimators, which specifies how many decision trees the BDT uses in the boosting process; the learning rate, which controls how much each tree contributes to the overall model; and the maximum depth of each decision tree. Careful tuning of these parameters is essential for achieving a balance between accuracy and generalization.

B. Improving BDT

To improve the performance of the BDT, several techniques are applied to enhance the model's training process and results.

First, before the training, loose filters are applied to the data to let the BDT focus on the more complex patterns and reduce the easy background noise. These filters are a loosened version of the filters discussed in section III. A full overview is given in App.C, Table VII C.

To prevent overfitting, the number of variables used by the BDT is limited through a feature selection process, which begins with a broad set of discriminant variables related to the particles involved in the decay. After training the BDT, the importance of each variable is determined based on how frequently it is used in the decision-making, and the least important variable is discarded. The smallest subset of variables that maintains an AUC value greater than 99% of the initial value is selected. On App.C Fig. 14 shows the evolution of the AUC value depending on the number of training variables, and Table VII C the final training variables.

Similarly, hyperparameters are optimized using the `GridSearchCV` function from the `sklearn` library. This function tests all combinations of a predefined grid of parameters and returns the set of parameters that yields the best AUC value. Based on this result, the BDT is trained with a learning rate of 0.15, 300 trees, and a maximum depth of 4.

Finally, K-fold cross-validation is employed. The dataset is divided into k equally-sized subsets, or "folds", in our case 5. The model is trained on $k-1$ folds and tested on the remaining one. This process is repeated k times, with each fold serving as the test set once. Finally, the results of each trained BDT are averaged, providing a more generalizable performance on unseen data compared to a single train-test split.

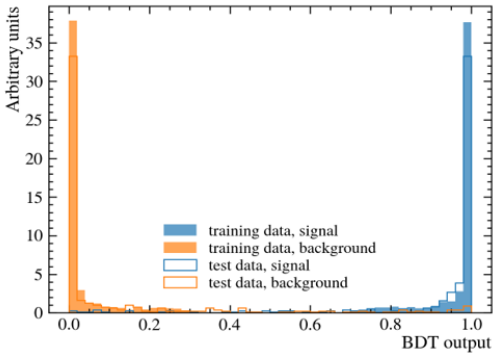

FIG. 3: BDT output for test and training data. Orange colour represents background and blue colour, signal.

The final performance of the BDT is shown in Figures 3 and 4. The model achieves an AUC value of 0.973. However, some overfitting is evident, as indicated by the AUC value of 1 for the training data and lower BDT output values for the test data.

C. BDT threshold

Once the BDT is trained, a threshold must be selected to classify events as signal or background, aim-

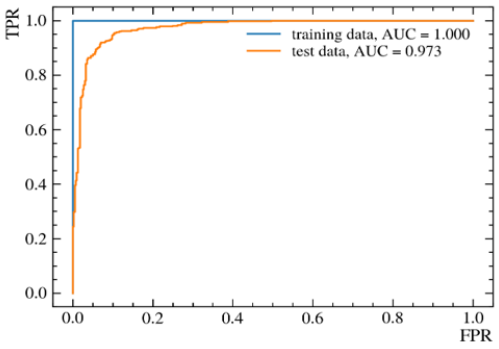

FIG. 4: ROC curve for training and test data. AUC value computed for training data = 1, test data = 0.973.

ing to balance the discarding of background while minimizing the loss of signal events (the evolution of signal and background for different BDT cuts is shown in Appendix C, Figures 16 and 17). To make this task, the maximum of a Figure of Merit (FOM), defined as $FOM = N_{sig}/\sqrt{N_{sig} + N_{bkg}}$, is chosen.
$N_{\rm sig}$ is calculated using the signal yield of the fit in the Ω_c^0 mass plot for the first BDT cut, 0.7, and then extended to the others as $N_{sig} = N_{sig}^{0.7} \frac{\varepsilon}{\varepsilon_{0.7}}$, where the efficiency, ε, is determined in simulation as $\varepsilon = N_{sig}^{after}/N_{sig}^{before}$. And $N_{\rm bkg}$ is the number of events classified as signal in a dataset outside the Ω_0^c mass peak after applying the BDT cut.

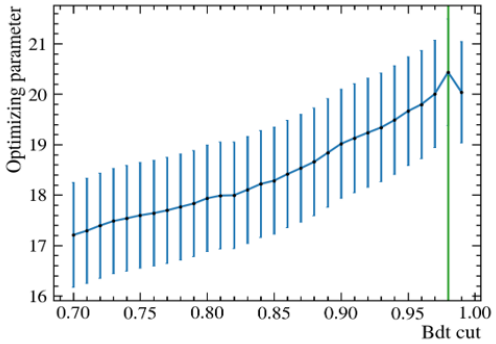

FIG. 5: FOM representation for different BDT cuts. The green line points out the optimal BDT cut = 0.98 with a corresponding FOM value = 20.4 ± 1.1.

Fig. 5 shows the evolution of the FOM value across different BDT cuts, which identifies a maximum corresponding to the optimal cut value, 0.98. The result of applying this cut and plotting Ω_c^0 mass is shown in Fig. 6.

The BDT selection is compared with the results obtained using the initial tight cuts, which have a FOM value of 12.75. At the optimal BDT point, the FOM increases to 20.4, demonstrating a significant improvement. App.C Fig. 18 shows the BDT-selected plot with a similar signal yield as Fig. 2. By comparing the two figures, it can be observed that the signal-to-background ratio has been improved by a factor of 2, while retaining the same amount of signal. Based on these results, we proceed to search for Ω^- resonances using the BDT selection.

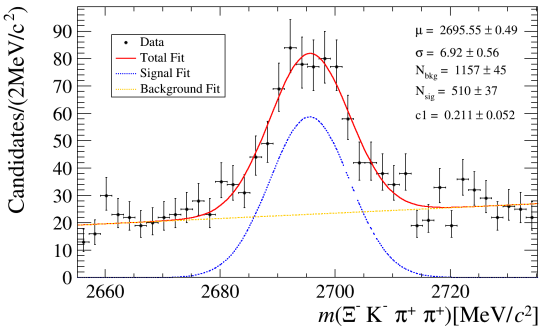

FIG. 6: Fitted Ω_c^0 mass variable with BDT cut 0.98 applied to the data. Gaussian fit for signal and linear for background.

D. Obtaining signal distributions from data

In the Ω_c^0 mass distribution, it is relatively easy to identify signal and background contributions. However, when analyzing other variables, separating signal from background becomes much more challenging. To overcome this, the technique *sPlot* [10] is employed, a statistical method that allows disentangling signal and background contributions in a dataset.

The *sPlot* technique relies on a Likelihood fit of the Ω_c^0 mass distribution, Fig. 6. A specific probability density function (PDF) has to be assumed for the shapes of the signal and background, in our case a Gaussian and a linear function. From this fit, a weight is assigned to each event, representing a probability of that event being signal. By applying these weights to the data, the signal distribution alone from the dataset is extracted.
The subsequent plots and results incorporate these weights, allowing focus on signal contributions while suppressing the background.

V. FINAL RESULTS

Resonant states of the particle Ω^- are searched by calculating the invariant mass of its decay products, $\Xi^- K^- \pi^+$. As the data sample represents to be pure signal, the resolution of the results is improved by substituting the calculated mass of the Ξ^- with its world-average mass of $1321.71\,\mathrm{MeV/c^2}$ [7].

Since there is information about two final pions from the Ω_c^0, but it is not known which one originates from the resonant state, the invariant mass is plotted using both pions.

The final plots are shown in Figures 7 and 8. It is difficult to identify significant signals due to the limited data and resulting fluctuations. However, between 2400

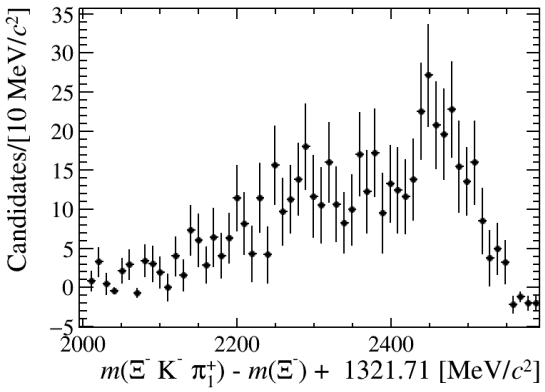

FIG. 7: Invariant mass spectrum for $\Xi^- K^- \pi_1^+$, with Ξ^- mass correction.

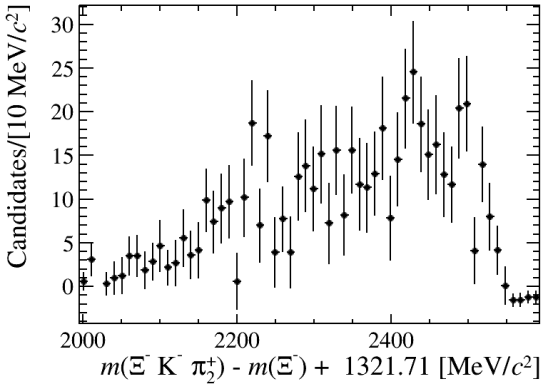

FIG. 8: Invariant mass spectrum for $\Xi^- K^- \pi_2^+$, with Ξ^- mass correction.

and 2500 MeV/c^2, there is a hint of a broad peak, which could be associated with the resonance $\Omega^-(2470)$ listed in PDG. With more data, this peak might become more pronounced, but at present, it is not significant enough to make definitive conclusions.

In App. D, the analysis of the decay chain $(\Omega^-)^* \to \Xi(1530)^0$ is presented by studying the $\Xi^- \pi^+$ spectrum, where the $\Xi(1530)^0$ resonant state is observed. The invariant mass of $\Xi^- K^- \pi^+$ is also calculated using data from the $\Xi(1530)^0$ peak, with an attempt to reduce background by excluding events in which the opposite pion originates from the $\Xi(1530)^0$ resonance.

VI. CONCLUSIONS

In this work, a BDT has been successfully developed to enhance the signal-to-background ratio in an LHCb data sample of the decay $\Omega_c^0 \to \Xi^- K^- \pi^+ \pi^+$. By comparing the results obtained with the BDT to those from tight selection cuts, the effectiveness of the method is demonstrated, as the signal-to-background ratio is increased by a factor of 2.

By applying the BDT and utilizing the *sPlots* technique, a substantial signal sample is obtained to calculate the invariant mass $m(\Xi^- K^- \pi^+)$ in the search for potential resonant states $(\Omega^-)^*$. While there is a hint of a broad peak in the mass range of 2400–2500 MeV/c^2, the limited size of the initial data sample results in insufficient statistical significance to confirm the existence of the resonant state.

In conclusion, it has been shown that this decay channel is a promising tool for the search of $(\Omega^-)^*$ resonances. Promising directions for future work should be studied. For instance, generating new simulation samples with higher statistics would improve the performance of the BDT; or incorporating data from additional LHCb runs would enhance the statistical power of the analysis, potentially revealing subtle features in the invariant mass distributions and leading to more robust conclusions about the existence of resonant states.

Acknowledgments

I am deeply grateful to my advisors, Carla Marin Benito and Lukas Calefice, for their guidance and encouragement throughout this project. I have learned so much from them during this journey.

[1] LHCb Collaboration, R. Aaij et al., *Observation of New Ω_c^0 States Decaying to the $\Xi_c^+ K^-$ Final State*, Phys. Rev. Lett. **131** (2023) 13, 131902, arXiv:2302.04733

[2] LHCb Collaboration, R. Aaij et al., *Observation of excited Ω_c^0 baryons in $\Omega_b^- \to \Xi_c^+ K^- \pi^-$ decays*, Phys. Rev. D **104** (2021) 9, L091102, arXiv:2107.03419.

[3] S. F. Biagi et al., *First Observation of Ω^* Resonances*, Z. Phys. C **31** (1986), UGVA-DPNC-113

[4] D. Aston et al., *Observation of Ω^{*-} Production in $K^- p$ Interactions at 11GeV/c*, Phys. Lett. B **194** (1987), SLAC-PUB-4132

[5] D. Aston et al., *Observation of a New Ω^{*-} at 2.47 GeV/c^2 in $K^- p$ Interactions at 11GeV/c*, Phys. Lett. B **215** (1988), SLAC-PUB-4657

[6] Belle Collaboration, J. Yelton et al., *Observation of an Excited Ω^- Baryon*, Phys. Rev. Lett. **121** (2018) 5, 052003, arXiv:1805.09384

[7] Particle Data Group, S. Navas et al., *Review of particle physics*, Phys. Rev. D **110** (2024) 3, 030001

[8] LHCb Collaboration, *The LHCb Detector at the LHC*, JINST 3 S08005 (2008), LHCb-DP-2008-001

[9] T. Chen and C. Guestrin, *XGBoost: A Scalable Tree Boosting System*, (2016), arXiv:1603.02754,

[10] M. Pivk and F. R. Le Diberder, *sPlot: a statistical tool to unfold data distributions*, Nucl. Instrum. Meth. A555 (2005), arXiv:physics/0402083.

Espectroscòpia de barions multiestranys en l'experiment LHCb al decaïment $\Omega_c^0 \to \Xi^- K^- \pi^+ \pi^+$

Author: Carla Garcia Gazulla
Facultat de Física, Universitat de Barcelona, Diagonal 645, 08028 Barcelona, Spain.

Advisor: Carla Marín Benito and Lukas Calefice

Resum: En aquest estudi s'analitza el decaïment $\Omega_c^0 \to \Xi^- K^- \pi^+ \pi^+$ per buscar estats excitats del barió Ω^-. Utilitzant dades de l'experiment LHCb, hem desenvolupat un Arbre de Decisió Potenciat que millora la ràtio senyal-fons en un factor 2 comparat amb criteris de selecció estàndard. Aquest enfocament ha resultat en un pic net de massa del barió Ω_c^0, que ens permet l'exploració dels estats excitats. L'espectre de massa invariant revela indicis d'una potencial ressonància.

Paraules clau: Física d'Altes Energies, Anàlisis de dades, machine learning, partícules estranyes, espectroscòpia
ODSs: Indústria, innovació, infraestructures

.

VII. APPENDIX

A. Track type

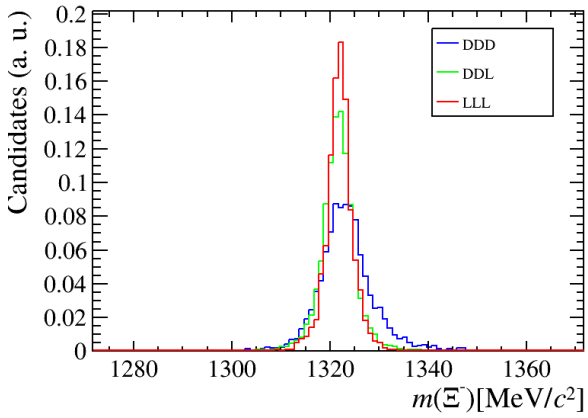

FIG. 9: Simulated signal distribution, normalized, for each track type for the variable Ξ^- mass.

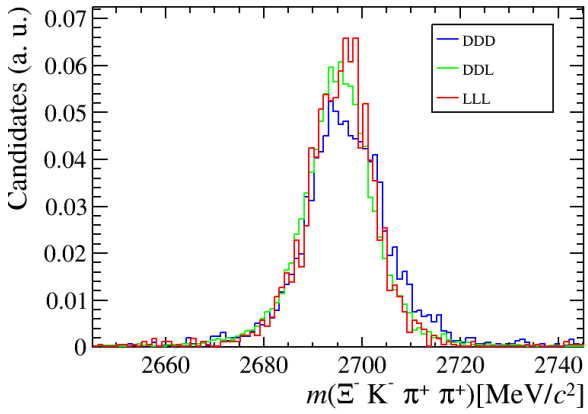

FIG. 10: Simulated signal distribution, normalized, for each track type for the variable Ω_c^0 mass.

Figures 9 and 10 show the differences in the resolution of Ξ^- and Ω_c^0 mass peaks, with DDD track type exhibiting a much broader peak compared to LLL, while DDL falls in between.
Comparing both plots, it can be seen that the difference is less significant for Ω_c^0, as it is reconstructed using all the final decay products, with three of them being always L tracks. This reduces the overall effect of track type differences. In contrast, for the Ξ^-, all its decay product tracks vary between DDD, DDL, and LLL configurations, amplifying the impact of track type differences.
For the final objective of this project, which involves calculating $m(\Xi^- K^- \pi^+)$, the effect of track types will be less pronounced compared to Fig. 9, since both π^+ and K^- are always L tracks.

B. Cuts

Variable	**Cut**
$\lvert m(\Omega_c^0) - 2695\,\mathrm{MeV/c^2}\rvert$	$< 50\,\mathrm{MeV/c^2}$
$p_\mathrm{T}(\Omega_c^0)$	$> 1500\,\mathrm{MeV/c}$
$p_\mathrm{T}(K^-)$	$> 400\,\mathrm{MeV/c}$
$p_\mathrm{T}(\pi_1^+(\Omega_c^0))$	$> 350\,\mathrm{MeV/c}$
$p_\mathrm{T}(\pi_2^+(\Omega_c^0))$	$> 350\,\mathrm{MeV/c}$
$\chi^2_{vtx}(\Omega_c^0)$	< 9
$\chi^2_\mathrm{IP}(K^-)$	> 2.4
$\chi^2_\mathrm{IP}(\pi_1^+(\Omega_c^0))$	> 1.9
$\chi^2_\mathrm{IP}(\pi_2^+(\Omega_c^0))$	> 1.9
$\cos(\theta_\mathrm{dir}(\Omega_c^0)$	> 0.9999
$\chi^2_{FD}(\Omega_c^0)$	> 15
$\chi^2_{FD}(\Xi^-)$	> 30
$\mathrm{ProbNN}\pi^+(\pi_1^+(\Omega_c^0))(1 - \mathrm{ProbNNK}(\pi_1^+(\Omega_c^0)))$	> 0.4
$\mathrm{ProbNN}\pi^+(\pi_2^+(\Omega_c^0))(1 - \mathrm{ProbNNK}(\pi_2^+(\Omega_c^0)))$	> 0.4
$\mathrm{ProbNNK}(K)(1 - \mathrm{ProbNN}\pi^+(K^-))$	> 0.25
$\lvert m(\Xi^-) - 1321\,\mathrm{MeV/c^2}\rvert$	$< 15\,\mathrm{MeV/c^2}$
$\lvert m(\Lambda^0) - 1115\,\mathrm{MeV/c^2}\rvert$	$< 10\,\mathrm{MeV/c^2}$

TABLE I: Selection cuts applied to the dataset

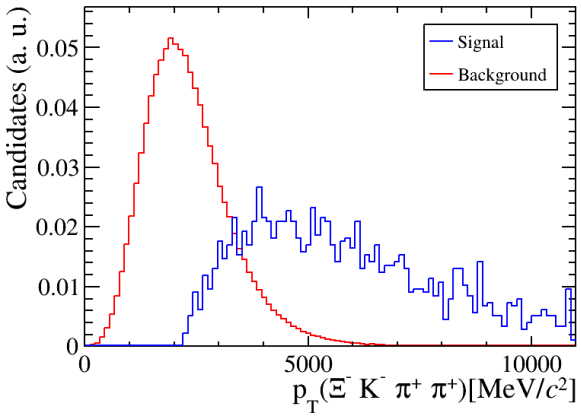

FIG. 11: Comparison between signal (from simulation) and background (from data outside Ω_c^0 mass peak) for the variable $p_\mathrm{T}(\Omega_c^0)$. Signal is plotted in blue, and background in red.

Table VII B provides a selection of cuts for various discriminant variables, designed to reduce the background while minimizing signal loss. Figures 11, 12, and 13 illustrate the distributions of signal and background for three examples of discriminant variables, demonstrating the effectiveness of the selected cuts.
As signal exhibits a higher momentum distribution than background, applying a cut on $p_T(\Omega_c^0) > 1500$ removes the majority of the background while retaining most of the signal. For $\chi^2_{vtx}(\Omega_c^0)$, the background displays higher values due to a poorer vertex fit. Imposing an upper limit of 9 on this variable helps significantly reduce the back-

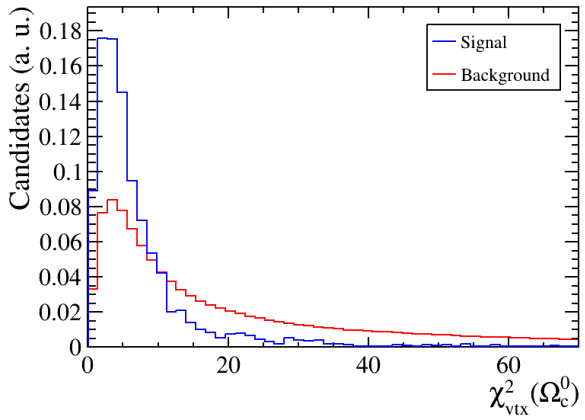

FIG. 12: Comparison between signal (from simulation) and background (from data outside Ω_c^0 mass peak) for the variable $\chi^2_{vtx}(\Omega_c^0)$. Signal is plotted in blue, and background in red.

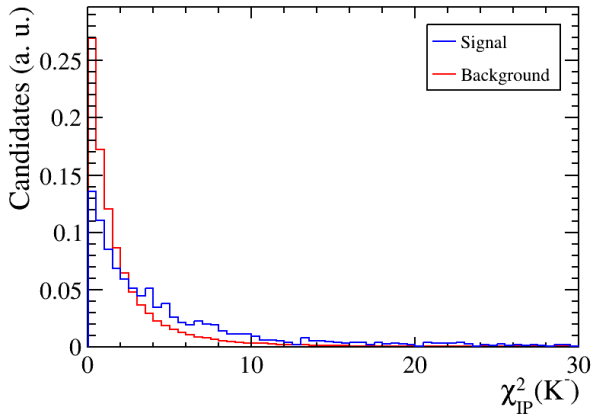

FIG. 13: Comparison between signal (from simulation) and background (from data outside Ω_c^0 mass peak) for the variable $\chi^2_{\rm IP}(K^-)$. Signal is plotted in blue, and background in red.

ground. As a final example, for χ^2 on the impact parameter of K^-, background candidates exhibit lower values. However, the cut is less clear, and some signal candidates are lost when imposing a lower limit of $\chi^2_{\rm IP}(K^-) > 2.4$.

C. BDT

Table VII C presents a loosened version of the cuts from Table VII B, applied to our data before BDT training.

Table VII C presents the list of variables used as input for the BDT to differentiate between signal and background. These variables are selected by progressively reducing a broad set to the smallest subset that retains an AUC value greater than 0.99 of the original list. Figure 14, shows the evolution of the AUC value as a function of the number of input variables.

Variable	**Cut**
$\lvert m(\Omega_c^0) - 2695\,\text{MeV/c}^2\rvert$	$< 100\,\text{MeV/c}^2$
$p_{\rm T}(\Omega_c^0)$	$> 2000\,\text{MeV/c}$
$p_{\rm T}(K^-)$	$> 400\,\text{MeV/c}$
$p_{\rm T}(\pi_1^+(\Omega_c^0))$	$> 250\,\text{MeV/c}$
$p_{\rm T}(\pi_2^+(\Omega_c^0))$	$> 250\,\text{MeV/c}$
$p_{\rm T}(\Xi^-)$	$> 1000\,\text{MeV/c}$
$\chi^2_{\rm vtx}(\Omega_c^0)$	< 20
$\chi^2_{\rm IP}(\Omega_c^0)$	< 0.1
$\chi^2_{\rm IP}(K^-)$	> 1
$\chi^2_{\rm IP}(\pi_1^+(\Omega_c^0))$	> 1
$\chi^2_{\rm IP}(\pi_2^+(\Omega_c^0))$	> 1
$\cos(\theta_{\rm DIRA}(\Omega_c^0))$	> 0.9995
$\chi^2_{\rm FD}(\Omega_c^0)$	> 10
$\chi^2_{\rm FD}(\Xi^-)$	> 20
$\text{ProbNNK}(\pi_1^+(\Omega_c^0))$	< 0.025
$\text{ProbNNK}(\pi_2^+(\Omega_c^0))$	< 0.025
$\text{ProbNN}\pi^+(\pi_1^+(\Omega_c^0))$	> 0.7
$\text{ProbNN}\pi^+(\pi_2^+(\Omega_c^0))$	> 0.7
$\text{ProbNNK}(K^-)$	> 0.6
$\text{ProbNN}\pi(K^-)$	< 0.3
$\lvert m(\Xi^-) - 1321\,\text{MeV/c}^2\rvert$	$< 15\,\text{MeV/c}^2$
$\lvert m(\Lambda^0) - 1115\,\text{MeV/c}^2\rvert$	$< 10\,\text{MeV/c}^2$

TABLE II: Loose cuts before BDT.

Variables	
$p_{\rm T}(\Omega_c^0)$	$\chi^2_{\rm IP}(\Omega_c^0)$
$\chi^2_{\rm FD}(\Omega_c^0)$	$\cos(\theta_{\rm DIRA}(\Omega_c^0))$
$\chi^2_{\rm vtx}(\Omega_c^0)$	$\chi^2_{\rm FD}(\Xi)$
$\cos(\theta_{\rm DIRA}(\Xi^-))$	$p_{\rm T}(\pi_1^+(\Omega_c^0))$
$\chi^2_{\rm IP}(\pi_1^+(\Omega_c^0))$	$\text{ProbNNK}(\pi_1^+(\Omega_c^0))$
$\text{ProbNN}\pi^+(\pi_1^+(\Omega_c^0))$	$\text{PIDK}(\pi_1^+(\Omega_c^0))$
$\text{GhostProb}(\pi_1^+(\Omega_c^0))$	$\chi^2_{\rm IP}(\pi_2^+(\Omega_c^0))$
$\text{ProbNNK}(\pi_2^+(\Omega_c^0))$	$\text{ProbNN}\pi^+(\pi_2^+(\Omega_c^0))$
$\text{PIDK}(\pi_2^+(\Omega_c^0))$	$\text{GhostProb}(\pi_2^+(\Omega_c^0))$
$\text{PIDK}(K^-)$	$\text{GhostProb}(K^-)$

TABLE III: List of variables BDT training, result of our feature selection.

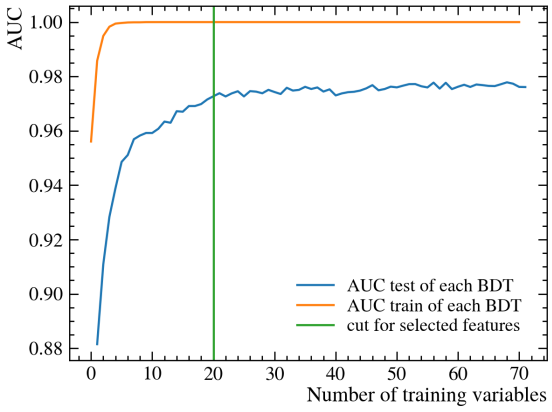

FIG. 14: AUC value of the trained BDT depending on the number of training variables. Green vertical line point out the selection made, twenty variables.

Fig. 15 shows the labelled data used to train the BDT. An equal number of events were selected for signal and background to prevent the BDT from favouring one class over the other. Background events were sampled from left and right of the Ω_c^0 mass peak to ensure the BDT learns to recognize different types of background.

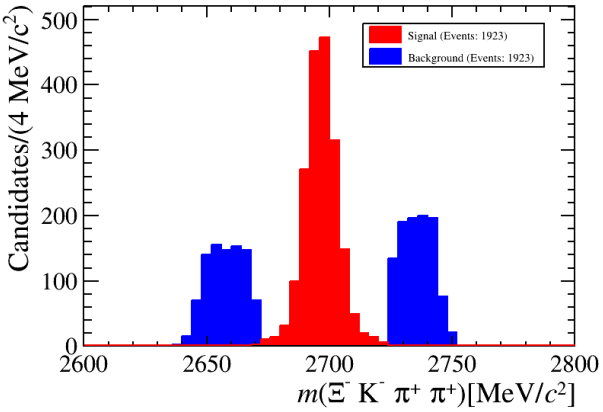

FIG. 15: Labelled data used to train the BDT.

Once the BDT is trained, different BDT cuts are applied to the entire dataset to evaluate their impact. Fig. 16 shows the number of background events misclassified as signal, which decreases linearly as the BDT cut value increases, as expected.

The number of signal events depending on the BDT cut is shown in Fig. 17. The plot reveals two distinct behaviours: a linear trend up to a cut value of 0.9, followed by a noticeable decrease in slope beyond that point. Based on these trends, the optimal BDT cut, which effectively reduces the background while minimizing signal loss, has to be identified.

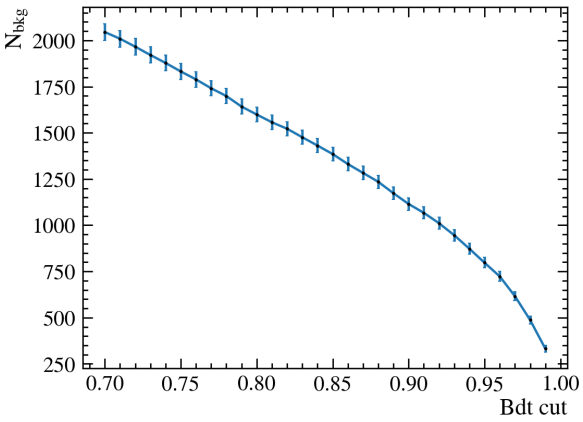

FIG. 16: Number of background events depending on BDT cut

To provide a meaningful comparison between the results of the initial tight cuts and the use of the BDT, a

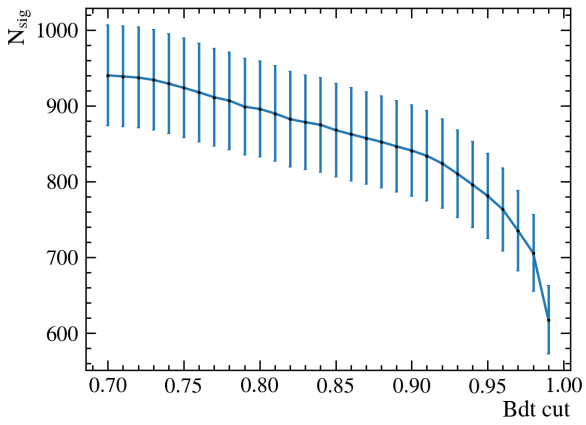

FIG. 17: Number of signal events depending on BDT cut

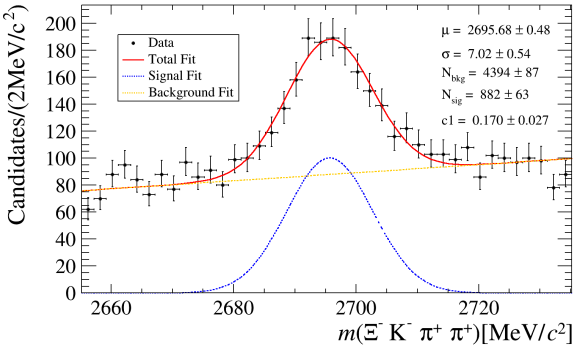

FIG. 18: Fitted Ω_c^0 mass variable with BDT cut 0.73 applied to the data. Gaussian fit for signal and linear for background

BDT cut that yields a similar number of signal events as the tight cuts is selected, 0.73. By comparing Figures 18 and 2, the improvement achieved is evident. The background yield is reduced from 8919 to 4394. While these numbers are approximations, the reduction is substantial enough to confidently demonstrate the effectiveness of the BDT approach over the tight cuts.

D. Extra analisis

1. Ξ^- resonant states

PDG lists some of the $(\Omega^-)^*$ states as decaying via the $\Xi(1530)^0$ resonance [7]. To study this process, we search for the presence of $\Xi(1530)^0$ states in our data, analysing the invariant mass spectrum of its decay products, $\Xi^-\pi^+$. In Figures 19 and 20, a pronounced peak in the mass range 1520–1560 MeV/c^2 can be observed, consistent with the expected resonance.

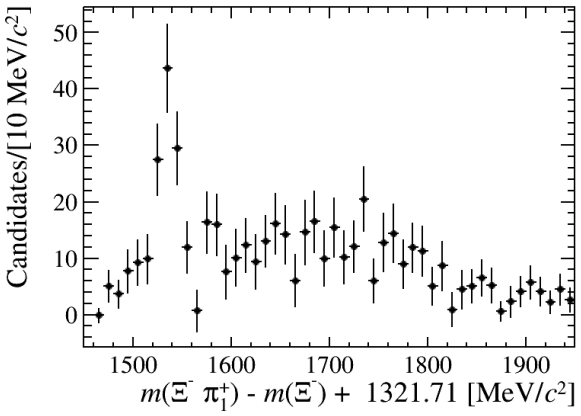

FIG. 19: Invariant mass spectrum for $\Xi^-\pi_1^+$, with Ξ^- mass correction

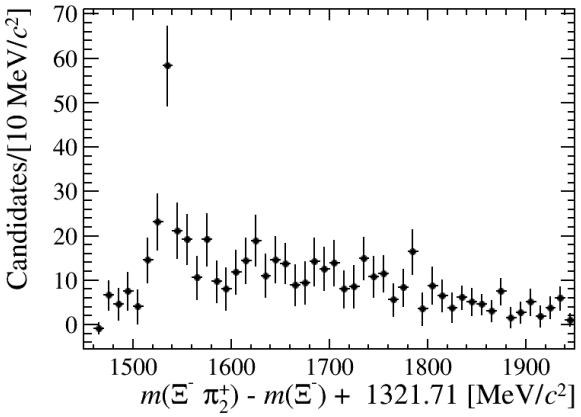

FIG. 20: Invariant mass spectrum for $\Xi^-\pi_2^+$, with Ξ^- mass correction

2. Ω^- resonant states to Ξ^- resonant state

To further analyse the previously mentioned possibility of the resonant state $(\Omega^-)^*$ decaying through the intermediate resonant state $\Xi^0(1530)$, data from Figures 19 and 20 within the region below 1600 MeV/c^2 (corresponding to the peak) is used to calculate the invariant mass $m(\Xi^- K^- \pi^+)$. The results, shown in Figures 21 and 22, indicate that too much data is lost, causing the peak between 2400 and 2500 MeV/c^2 to disappear.

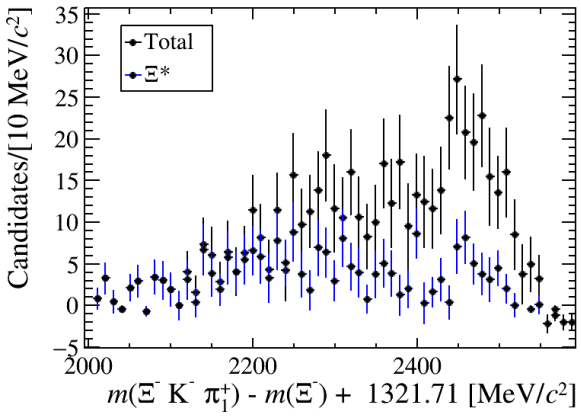

FIG. 21: Invariant mass spectrum for $\Xi^-K^-\pi_1^+$, with Ξ^- mass correction. In black for all the data, and in blue for the data that later forms a $\Xi^0(1530)$ resonance.

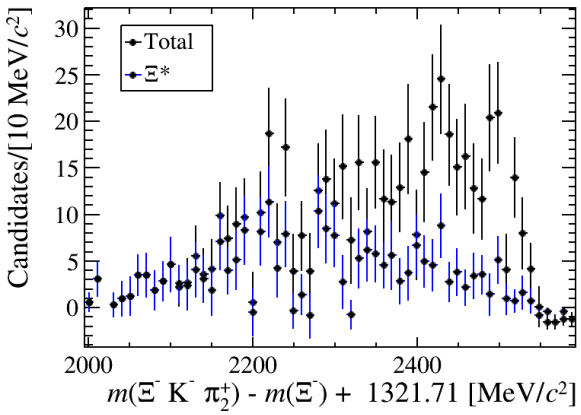

FIG. 22: Invariant mass spectrum for $\Xi^-K^-\pi_2^+$, with Ξ^- mass correction. In black for all the data, and in blue for the data that later forms a $\Xi^0(1530)$ resonance.

3. Ω^- resonant states deleting background Ξ^- resonant state opposite pion

In this section, an attempt to eliminate a portion of the background is presented. If the opposite pion being studied forms a $\Xi^0(1530)$ resonant state, the invariant mass under consideration will not form any $(\Omega^-)^*$ resonant state. Not only does the event lack of relevance, but it may also introduce a confusing peak in our spectrum. To address this, the data where the opposite pion lies within the $\Xi^0(1530)$ peak is excluded.

The results, shown in Figures 23 and 24, suggest that instead of removing background, the available phase

space for the invariant mass at higher values has been reduced. This may occur because the decay does not have enough energy for the second pion to achieve high energies and form a resonant state with the first pion (or the other way around).

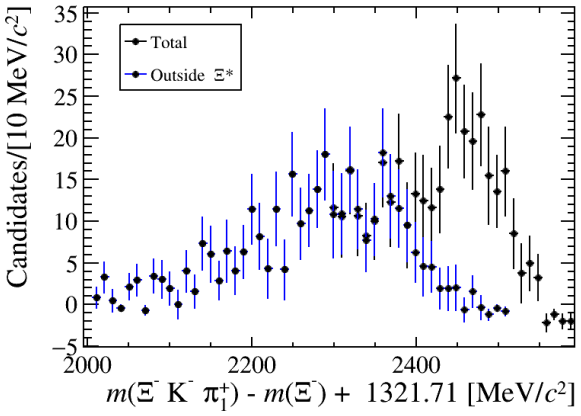

FIG. 23: Invariant mass spectrum for $\Xi^- \pi_1^+$, with Ξ^- mass correction. Black for all the data, and blue for the data where the second pion is outside $\Xi^0(1530)$ peak.

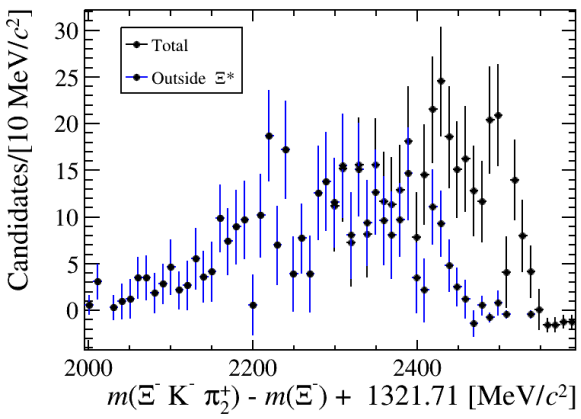

FIG. 24: Invariant mass spectrum for $\Xi^- \pi_2^+$, with Ξ^- mass correction. Black for all the data, and blue for the data where the first pion is outside $\Xi^0(1530)$ peak.